High-resolution two-phase velocimetry of aspherical particles using wavelet-based optical flow velocimetry (wOFV) benchmarked with fully resolved direct numerical simulations

Christopher Geschwindner[1,*], Maren Werner[1], Laurent André[2], Alexander Nicolas[3], Brian Peterson[3], Matthias Meinke[2], Wolfgang Schröder[2], Andreas Dreizler[1], Benjamin Böhm[1]

1: Technical University of Darmstadt, Department of Mechanical Engineering, Reactive Flows and Diagnostics, Otto-Berndt-Str. 3, 64287 Darmstadt, Germany
2: RWTH Aachen University, Chair of Fluid Mechanics and Institute of Aerodynamics, Wüllnerstr. 5a, 52062 Aachen, Germany
3: University of Edinburgh, School of Engineering, Institute of Multiscale Thermofluids, The King's Buildings, Edinburgh EH9 3FD, United Kingdom
*Corresponding author: geschwindner@rsm.tu-darmstadt.de

Keywords: Multi-phase velocimetry, Optical flow, Particle rotation, Aspherical particles.

ABSTRACT

Several techniques exist to measure the carrier and dispersed phases in multi-phase flows. Particle image velocimetry (PIV) analyzes the carrier phase by cross-correlating particle images, but its resolution is limited by the size of the interrogation window, making it difficult to resolve fine-scale turbulent structures. Particle tracking algorithms capture translational motion of dispersed particles well, but struggle with rotational motion, especially for irregular and aspherical particles. Currently, there is no method that universally measures both the carrier phase velocity field and the translational and rotational motions of dispersed particles. This study evaluates wavelet-based optical flow velocimetry (wOFV) for motion estimation in multi-phase flows, focusing on dispersed ellipsoidal particles and their surrounding turbulent carrier flow using synthetic image data. The research proceeds in two phases: first, the rigid motion of ellipses, including translational and rotational components, is analyzed using wOFV-generated dense motion fields. The results highlight the critical role of the regularization weighting parameter λ. Higher λ values improve translational motion estimation, while an optimal λ avoids under-regularization and non-physical structures in rotational motion. wOFV maintains accuracy in combined motion scenarios with optimal λ values. In the second phase, wOFV captures the turbulent carrier flow around an aspherical particle, benchmarked against DNS data and compared to PIV. wOFV outperforms PIV in resolving finer structures near the particle surface and in accurately representing the wake region. Error analyses confirm wOFV's superior performance, with optimal results within a specific λ range. In conclusion, wOFV is a highly effective tool for the analysis of multi-phase flow dynamics, providing greater resolution and accuracy than PIV, especially in complex scenarios involving aspherical particles.

1. Introduction

Simultaneously capturing the movement of dispersed particles and their encompassing turbulent carrier flow is pivotal for understanding the intricate interactions that modulate both particle and

flow dynamics. The inherent non-sphericity of many particles, such as those found in biomass combustion or the pneumatic transport of fibers, introduces an additional layer of complexity to these systems (Voth & Soldati, 2017; Panahi et al., 2019). Accurate capture of particle-turbulence interactions demands the development of precise particle-resolved experimental and numerical methods. In numerical investigations of particle-laden turbulent flows, the common approach employs an Euler-Lagrange framework, treating the dispersed phase as point particles and not fully resolving their interactions with the turbulent carrier phase (Balachandar & Eaton, 2010). For non-spherical biomasses, this method requires detailed knowledge of drag and torque characteristics, which are shape- and orientation-dependent within the flow field. These specifics are often obtained from highly-resolved single-particle simulations, as exemplified by the authors in a prior study (Fröhlich et al., 2020). However, the extreme computational effort of fully resolved simulations for particle-laden turbulent flows at high Reynolds numbers underscores the compelling necessity for high-resolution experimental methods in such environments.

Various strategies exist for experimentally measuring the carrier and dispersed phases simultaneously. In this study, we will focus exclusively on planar techniques, which, despite the significant advancements in three-dimensional measurement technologies, remain predominant due to their widespread usage and ease of implementation. A straightforward approach involves seeding the carrier phase with ideally following tracer particles. The scattered light of an incident laser sheet illuminating both tracer and large particles is captured using a single camera. Subsequently, both phases are separated using image discrimination algorithms based on differences in light intensity and particle size (Schmidt & Sutton, 2020). The processing of the carrier phase commonly employs particle image velocimetry (PIV), which involves cross-correlation of particle images within interrogation windows across consecutively recorded frames (Raffel et al., 2018). However, the spatial resolution of the resulting vector field is confined by the dimensions of the interrogation window, presenting a hurdle in effectively resolving small-scale turbulent structures (Kähler et al., 2012). Velocity measurements of large particles within the dispersed phase typically rely on a particle tracking algorithm. These algorithms either track a reference point (e.g., the centroid) or operate via cross-correlation, akin to particle image velocimetry. While effective in capturing translational motion, challenges emerge when addressing the rotational movement of aspherical particles. Particle rotation cannot be captured by cross-correlation methods when the interrogation window is larger than the particle size, as the rotational movement of a rigid body translates into a velocity gradient across the particle. An alternative approach to quantify rotational speeds involves fitting a suitable shape onto the particle image and tracking its orientation over time, as demonstrated by the authors for ultra-high-speed measurements of fibrous aspherical biomasses in a previous investigation (Geschwindner et al., 2023). Nonetheless, it is evident that there is currently no universally applicable approach to measure both the carrier phase velocity field and the translational and rotational movement of aspherical dispersed particles.

A novel approach to flow velocimetry are methods based on optical flow, which have the capability

to yield dense motion fields, generating a vector per pixel. An advanced form within this category is wavelet-based optical flow velocimetry (wOFV), incorporating an inherent multi-scale process within its mathematical framework (Kadri-Harouna et al., 2013; Dérian et al., 2013). Demonstrating superior accuracy in processing tracer particle images derived from direct numerical simulations (DNS) of turbulent flow fields, these methods outperform state-of-the-art PIV codes as demonstrated in diverse scenarios, including homogeneous isotropic turbulence (Schmidt & Sutton, 2019) and wall-bounded flows (Nicolas et al., 2023; Jassal & Schmidt, 2023). While dense motion fields have demonstrated potential in capturing small-scale structures in turbulent fluid motion, the comprehensive measurement of the rigid motion of aspherical particles within a flow field using optical flow methods has not yet been explored. This study introduces a novel application of wOFV for measuring both the carrier and dispersed phase movements in a unified framework.

To rigorously test and validate the wOFV algorithm for multi-phase motion estimation, our methodological design proceeds in two distinct phases:

1. **Rigid motion estimation of aspherical particles:** Initially, we simulate ellipsoids moving in a plane without a carrier flow to focus solely on the capability of wOFV to extract large particle motions. This step serves to establish the baseline accuracy and efficiency of wOFV in tracking simple translational and rotational movements of isolated ellipsoidal particles.

2. **Multi-phase flow simulation and carrier-phase turbulence estimation:** Building on the work of (Fröhlich et al., 2020), we perform a DNS of an ellipsoidal particle immersed in a turbulent carrier flow. From this DNS, synthetic tracer particle images are generated and then segmented into fluid and dispersed phases. These segmented images are processed with wOFV to assess the efficacy of the algorithm to estimate the dynamic turbulent carrier phase surrounding the particle.

To validate our approach, we compare the wOFV-processed synthetic data from both phases against ground truths derived from their respective simulations. Additionally, we benchmark the results of the fluid phase against those obtained using a state-of-the-art PIV code.

In the subsequent section, we provide a concise overview of the optical flow method utilized and its application within the multi-phase velocimetry framework developed for this study. Furthermore, we will illustrate how synthetic images are generated for both ellipsoidal particles and their surrounding turbulent flow, using the data obtained from DNS.

2. Methods

2.1. Wavelet-based optical flow velocimetry (wOFV)

The general principle of optical flow techniques for velocimetry is the conservation of the brightness intensity $I(\underline{x}, t)$, which is expressed as the optical flow constraint equation:

$$\frac{\partial I(\underline{x}, t)}{\partial t} + \underline{u}(\underline{x}, t) \cdot \nabla I(\underline{x}, t) = 0. \tag{1}$$

When integrated over a unit time interval, Eq. (2) computes the displaced frame difference. This term establishes the correlation between the measured intensity $I(\underline{x}, t)$, and the desired two-dimensional displacement vector field, denoted as $\underline{u}(\underline{x}, t)$. Effectively, this equation states that the spatial intensity distribution of the second image I_1 can be mapped onto the first image I_0 using the displacement field $\underline{u}(\underline{x})$, such that their difference vanishes. In other words, a minimization of Eq. (2) leads to an ideal dewarping solution.

$$I_0(\underline{x}) - I_1(\underline{x} + \underline{u}(\underline{x})) = 0 \tag{2}$$

However, this data term is ill-posed as it connects two velocity components, treated as unknowns, to a single observable variable being the local intensity. This issue is also known as the aperture problem (Heitz et al., 2010), where local motion can only be reliably estimated in the direction of the intensity gradient in the absence of distinguishable features. To address this challenge, variational approaches undertake a minimization of the data term within a penalty function, forming J_D (Horn & Schunck, 1981). This process is coupled with a regularization term, J_R, which solely depends on the derivatives of the velocity field. The concurrent minimization of J_D and J_R results in a well-posed convex optimization problem for computing the estimated displacement field $\hat{\underline{u}}$ as expressed in Eq. (3).

$$\hat{\underline{u}} = \arg\min_{\underline{u}} J_D(I_0, I_1, \underline{u}) + \lambda \, J_R(\underline{u}) \tag{3}$$

In the literature, a multitude of regularization terms are found depending on the application of the optical flow algorithm. For turbulent fluid flows with high levels of vorticity, a penalization of second-order derivatives in the form of a Laplacian is commonly used, which is as well employed in this study (Kadri-Harouna et al., 2013; Nicolas et al., 2023): $J_R = \int_\Omega |\nabla^2 u_1|^2 + |\nabla^2 u_2|^2 \mathrm{d}\Omega$. The scalar parameter λ, often termed regularization weighting parameter, determines the weighting balance between J_R and J_D, with higher values promoting increased smoothness in the estimated displacement field.

wOFV differs from traditional OFV methods by performing minimization in the wavelet domain rather than the spatial domain, as shown in Eq. 4. This minimization involves the wavelet coeffi-

cients $\underline{\theta} = (\theta_1, \theta_2)^T$, using the discrete wavelet transform (DWT), represented as $\underline{\theta} = \Psi^{-1}(\underline{x})\ \underline{u}$.

$$\hat{\underline{\theta}} = \arg\min_{\underline{\theta}} J_D(I_0, I_1, \underline{\theta}) + \lambda\ J_R(\underline{\theta}) \tag{4}$$

The minimization is performed over multiple scales in the wavelet domain, which is inherently a multi-resolution approach (Kadri-Harouna et al., 2013). This technique has been validated to effectively resolve the wide range of length scales in turbulent flows for several flow configurations (Dérian et al., 2013; Schmidt & Sutton, 2019; Nicolas et al., 2023). Furthermore, recent research has shown that wOFV outperforms PIV over a wide range of λ values (Nicolas et al., 2023) for the estimation of turbulent wall-bounded flows. It is therefore of great interest to see the performance of wOFV for both the estimation of the surrounding carrier turbulence and the particle motion itself.

2.2. Rigid motion estimation of ellipsoidal particles from dense motion fields

Previous research has utilized wOFV to estimate fluid velocities from tracer images. However, an intriguing extension is to determine if it is possible to extract the rigid motion of a solid particle from a dense motion field generated using optical flow velocimetry methods. For a planar image, the motion of a solid body can be decomposed into translational velocity $\underline{u}_p$ and angular velocity ω_p around the z-axis. Although any point on the solid body can theoretically be used for this analysis, it is practical to use the centroid c to determine $\underline{u}_c = \underline{u}_{p,c}$ for the translational velocity. Using this definition, rotation is defined around the center point $[x_c, y_c]$. If the translational velocity of the center point and the angular velocity are known, the velocity $\underline{u}_i$ for each point on the solid body is given by

$$\underline{u}_i = \underline{u}_{p,c} + |\underline{r}_{ci}|\ \omega_p\ \underline{e}_{\varphi,i}, \tag{5}$$

where $\underline{r}_{ci}$ is the vector from position i to the center point, and $\underline{e}_{\varphi,i}$ is the unit vector perpendicular to $\underline{r}_{ci}$. In images, point i represents individual pixels covered by the particle. All quantities are illustrated in Fig. 1(e). Based on this definition, multiple ways exist to reverse this computation, i.e. to compute $\underline{u}_c$ and ω_p from the dense motion field $\underline{u}_i$ from i pixels covering the particle surface in pixel space. Prior to the work presented in this paper, we have compared different solution methods by first computing 2000 individual ideal vector fields for a synthetic simulated ellipsoid (shown in Fig. 1(a-d)). Second, wOFV was computed using the synthetic rendered pixel image pair representatively shown in Fig. 1(a), resulting in a dense motion field deviating from the ideal solution. While a direct solution of the overdetermined system of equations based on Eq. (5) is technically possible using a least-squares approach, the most accurate results were yielded through first calculating a translational velocity based on the mean velocity of all N particle-covered pixels

$$\hat{\underline{u}}_{p,c} = \frac{1}{N}\ \sum_i \hat{\underline{u}}_i, \tag{6}$$

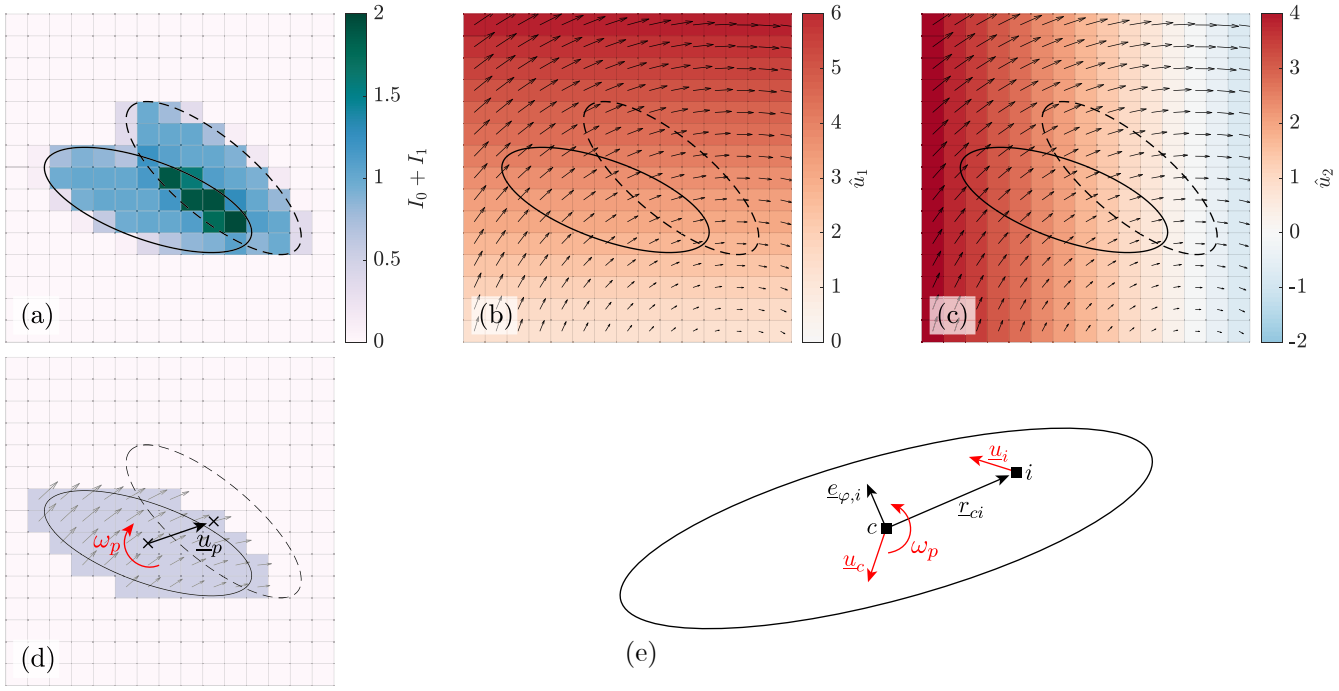

Figure 1. Synthetic image generation and motion estimation of ellipse particles using wOFV. (a) Synthetic pixelated images of moving ellipses. (b,c) Corresponding ideal dense motion fields. (d,e) Visualization of rigid motion estimation from dense motion fields.

and computing the rotational velocity afterwards using

$$\hat{\omega}_{p,i} = \left| \frac{(\underline{\hat{u}}_i - \underline{\hat{u}}_{p,c})_\perp}{|\underline{r}_{ci}|} \right|. \tag{7}$$

This approach results in a solution $\hat{\omega}_{p,i}$ for each individual pixel covered by the particle. Subsequently, we found that the most accurate results for a representative angular velocity were computed using the mode value of $\hat{\omega}_{p,i}$ for all particle-covered pixels. As will be discussed and shown in Section 3.1.2, median and mean values lead to a systematic underestimation of $\hat{\omega}_p$ due to the aperture problem. In summary, rigid body motion can be extracted from a dense motion field using Eq. (6) for the translational velocity and Eq. (7) for the angular velocity. A systematic study exploring the capabilities of wOFV to extract these parameters for aspherical ellipses is reported in Section 3.1.

2.3. Particle-resolved DNS and synthetic tracer image generation

Direct numerical simulation A prolate spheroid with an aspect ratio of 4 and an equivalent diameter of D_{eq} immersed in a turbulent carrier flow is investigated and compared to a highly-resolved direct particle-fluid simulation (DPFS). For the particle-resolved reference simulation, a finite-volume solver with hierarchically refined Cartesian meshes is employed. The solver has been

validated in several studies (Hartmann et al., 2011; Schneiders et al., 2017; Fröhlich et al., 2020). The inviscid fluxes are computed through an upwind-biased scheme, while a central scheme is applied for the viscous fluxes. For the time integration, an explicit five-stage predictor-corrector Runge–Kutta method is used (Schneiders et al., 2016). The computational cost of the simulation is significantly reduced through adaptive mesh refinement, where the mesh is refined only in the vicinity of the particle based on a distance sensor. The particle surface is sharply described by a signed-distance or level-set function and discretized by means of a cut-cell method. Conservation is ensured through a flux-redistribution technique that stabilizes the inherently small cut-cells (Schneiders et al., 2016). As inflow boundary condition, a random eddy inflow method similar to Batten et al. (2004) is implemented to provide realistic turbulent inflow conditions. Random eddies are generated to match the specified inlet turbulence intensity of 10 %. Pressure is extrapolated while the freestream value is prescribed for the density. Since there is no production of turbulence, the turbulence intensity is decaying naturally along the streamwise direction. At the outflow, a boundary condition of Neumann type is imposed to ensure that the flow exits without generating spurious pressure waves back into the computational domain. For the lateral directions, periodic boundary conditions are applied in the y- and z-direction, mimicking the simulation of an infinite domain in these directions. The ellipsoidal particle is fixed at $15D_{eq}$ downstream of the inlet until statistical convergence for the flow field is reached. Then, the particle is released with the translational movement restricted to the xz-plane and the rotation restricted to the out-of-plane axis. The grid resolution is selected such that $D_{eq}/\Delta_{min} = 40$ with a total of 288 million cells within a domain of size $(80D_{eq}\times 20D_{eq}\times 20D_{eq})$. Figure 2(a) shows a zoomed-in snapshot of the flow field, highlighting the turbulent flow around the prolate spheroid.

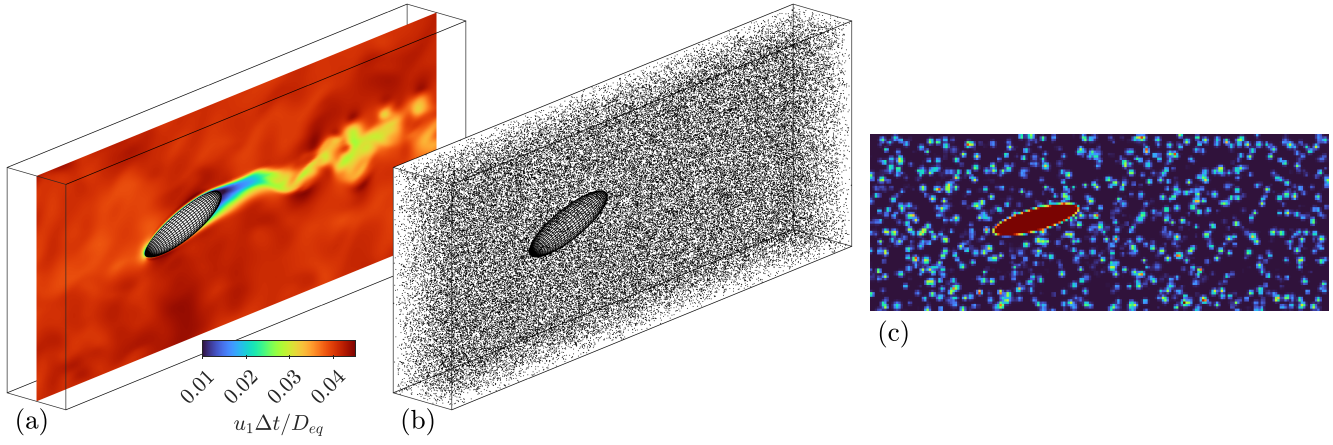

Figure 2. Synthetic image generation from DPFS. (a) Center slice of a representative time-step of the DPFS with (b) a corresponding snapshot of tracers positioned in the domain of interest. (c) Exemplary synthetic rendered multi-phase Mie scattering image for motion estimation.

Synthetic image generation To generate synthetic images from DNS data, the tracer particles are randomly distributed in the domain to generate the first synthetic image. The motion of these tracer particles for subsequent images is computed based on the velocities provided by the DNS data set. Similar to Nicolas et al. (2023), the displacement of each particle in each second frame is computed numerically using an explicit Runge-Kutta scheme, with linear interpolation applied to the particle positions. The physical positions of the particles are then scaled to pixel coordinates to fit within the image frame. Each particle is assigned maximum intensity values based on its out-of-plane position within the laser sheet, ensuring that particles closer to the focal plane have higher intensity values. The thickness of the laser sheet is characterized by $\sigma_{LS} = 2.1$, which corresponds to a laser sheet thickness of 0.33 D_{eq} or 50 µm for an equivalent particle diameter of 150 µm. The size distribution of the tracer particles is adjusted to follow a log-normal distribution, ensuring that the tracers cover approximately 2 pixels in size. The in-plane intensity distribution for each particle is computed from the integral of a two-dimensional circular Gaussian distribution, modeling the intensity spread of the particle within the image. The calculated intensity values are then scaled and discretized to fit a 12-bit camera sensor. Finally, the images are padded to a square image size of $2^k \times 2^k$ with $k \in \mathbb{N}$ for wOFV processing.

3. Results and Discussion

3.1. Large particle motion estimation using wOFV

The first analysis focuses on the motion of large ellipsoidal particles using wOFV. The goal is to assess how accurately wOFV can estimate the translational and rotational motion of the particles by comparing the estimated motion parameters $\hat{\underline{u}}_p$ and $\hat{\omega}_p$ with the ground truth values $\underline{u}_p$ and ω_p. Table 1 outlines the parameter settings for this study. Ellipsoids with an aspect ratio of 4 are generated and randomly placed within a square domain. These particles are then moved according to predefined constraints, and the contours are rendered on a pixel grid at two successive time steps. The resulting image pairs are processed by the wOFV algorithm with different regularization weights λ. Finally, the translational and rotational motions are estimated using the method described earlier in Section 2.2.

3.1.1. Translational motion

To start with the simplest case, we examine purely translational motion. Here, single ellipsoids are randomly placed in the domain and only translate in the image plane. The boundary conditions listed in Table 1 apply except for the rotational motion, which is set to $\omega_p = 0^\circ$ for all particles. Figure 3 shows the estimated translational velocity plotted against the ground truth for four λ regularization weighting parameters. As can be seen, increasing values of λ lead to a better ap-

Table 1. Parameters for the study of ellipsoidal particle motion tracked by wOFV. If not declared differently, all numbers are given in units of pixels.

Parameter	Value	Processing Step
Number of image pairs	1000	Synthetic image generation
Image size	128×128	Synthetic image generation
Ellipsoid size	$a = 20$, $b = 5$	Synthetic image generation
Initial centroid position	$[x_c, y_c] \in \{x \mid 40 \leq x \leq 88\}$	Synthetic image generation
Initial orientation	$\pm$ 90°	Synthetic image generation
$\underline{u}_p$	$\pm$ 0 – 12	Synthetic image generation
ω_p	$\pm$ 0° – 40°	Synthetic image generation
Reg. scheme	Laplacian	wOFV
Reg. weighting λ	{0.01, 0.1, 1, 10, 100}	wOFV

proximation of the translational velocity of the ellipsoids over all displacement values. Notably, for all λ values, the deviations from the ground truth are largely independent of the displacement value. It was also observed that the wOFV algorithm consistently found an appropriate solution as long as the particle images overlapped between frames. For cases where particle images do not overlap, employing a simple centroid tracking algorithm before wOFV estimation can generate an initial condition, effectively removing any limitations on the estimated translational displacement.

These observations can be explained by considering the nature of the flow field of a purely translational particle against a dark background. In such a scenario, the flow field is uniform in space, meaning that gradients do not appear in an ideal solution between neighboring vectors in the dense motion field. Consequently, higher values of the regularization weighting parameter λ enhance the accuracy of the tracking method by promoting smoothness in the estimated velocity field. Therefore, for pure translational motion of a single object in the domain, it is advisable to use a high value for λ. It should be noted, however, that this recommendation may change when tracking multiple rigid bodies, even if their motion is purely translational. For our specific case and given the range of observed values, the higher the λ, the better the performance of wOFV.

3.1.2. Rotational motion

Following the analysis of translational motion, we now examine pure rotational motion. Ellipsoids are randomly placed in the domain and subjected to rotation without any translational movement. Accordingly, the boundary conditions detailed in Table 1 are valid apart from the translational motion, which is set to $\underline{u}_p = 0$ px for all particles. Figure 4 shows the estimated angular velocity plotted against the ground truth for six regularization weightings λ. As indicated in the figure, the devia-

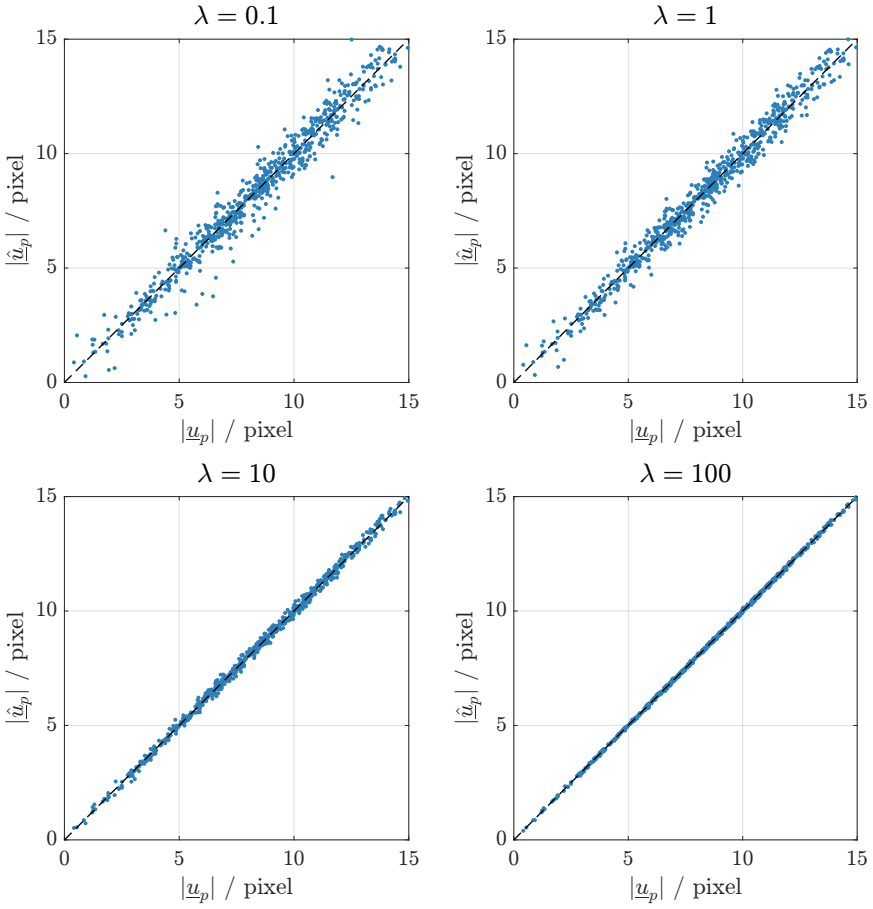

Figure 3. wOFV-based tracking of 1000 individual ellipsoids undergoing purely translational motion. Computed translational velocity magnitude $|\underline{\hat{u}}_p|$ compared to true velocity magnitude $|\underline{u}_p|$ for different regularization weighting parameters λ.

tion between the estimated angular velocity $\hat{\omega}_p$ and the true angular velocity ω_p increases with the magnitude of the angular velocity. This effect is particularly pronounced for higher regularization weighting parameter, where the underestimation of ω_p becomes more significant.

The observed behavior can be attributed to the necessity of resolving velocity gradients in the flow field of a purely rotating particle. Unlike translational motion, rotational motion inherently involves velocity gradients around the center of rotation. When the regularization weighting parameter λ is set too high, these essential gradients are smoothed out, leading to inaccuracies in the estimated angular velocity, particularly evident in an increasing underestimation of the angular velocity as $|\omega_p|$ increases. Conversely, setting λ too low can result in nonphysical outliers in the vector field, causing a wider spread of samples, as observed for $\lambda = 0.001$.

The limit of wOFV regarding the maximum predictable angular velocity is not as clearly defined as in the case of translational motion. For pure rotation, the overlap between the ellipsoid in successive frames I_0 and I_1 is always guaranteed. However, the absolute error in angular velocity

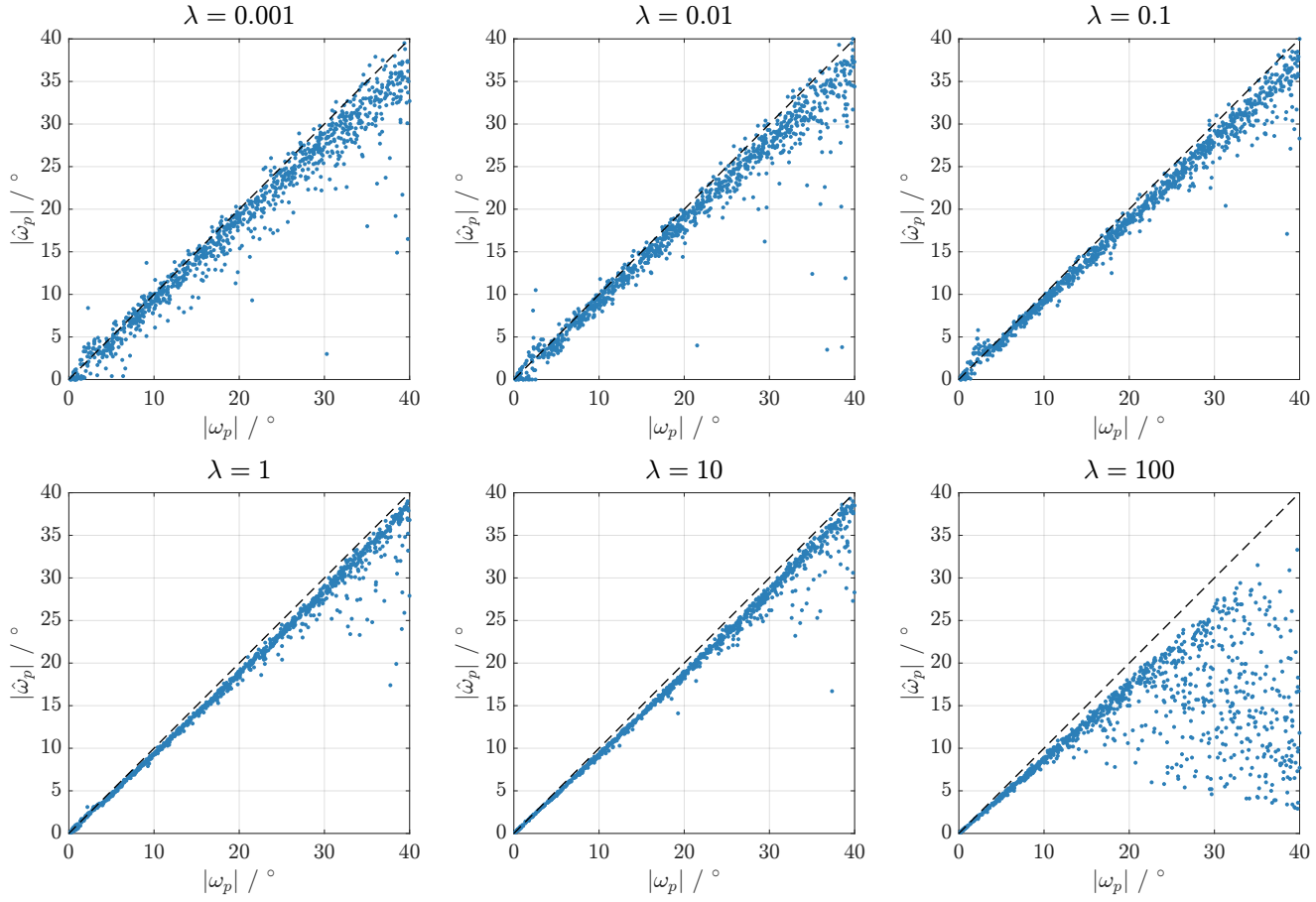

Figure 4. wOFV-based tracking of 1000 individual ellipsoids undergoing pure rotational motion. Computed angular velocity magnitude $|\hat{\omega}_p|$ compared to the true angular velocity magnitude $|\omega_p|$ for different regularization weighting parameters λ.

estimation increases with the magnitude of the angular velocity. Furthermore, there is a threshold angular velocity ω_{th} above which the algorithm fails to provide meaningful predictions, especially for high regularization values. The threshold ω_{th} depends strongly on the regularization weighting parameter λ. For example, the performance of the algorithm differs significantly between $\lambda = 10$ and $\lambda = 100$. To quantify ω_{th}, one could iteratively compute a linear fit through the samples with $\omega_i < \omega_{max}$. By incrementing ω_{max} and evaluating the mean squared error (MSE) of the fit, ω_{th} can be identified as the value of ω_{max} where MSE exceeds a predefined maximum.

Given the results for ellipses with an aspect ratio of 4, it is interesting to investigate the effect of varying the aspect ratio on the rotational motion estimation. Therefore, additional simulations of ellipsoids with different aspect ratios but similar particle areas of $A = 100\pi$ (in units of pixels) were performed for all investigated λ values. A representative ellipse with identical initial orientation and angular velocity but varying aspect ratio is shown in Figure 5(a-d) for a regularization weighting parameter of $\lambda = 10$. Here, the distribution of the median relative error of the angular velocity

estimation $(\hat{\omega}_{p,i} - \omega_p)/\omega_p = \Delta\omega_p/\omega_p$ is shown on the surface of all ellipses examined. Regions of underestimation are indicated by negative values, while positive values indicate overestimation.

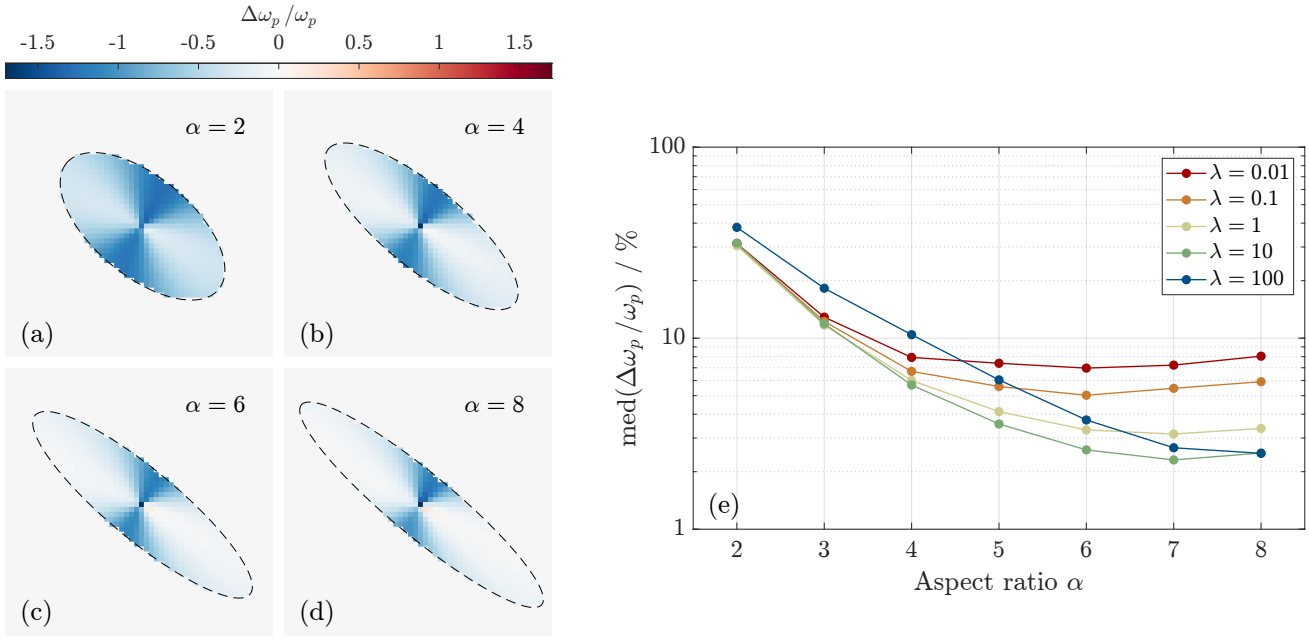

Figure 5. (a-d) Distribution of $(\hat{\omega}_{p,i} - \omega_p)/\omega_p = \Delta\omega_p/\omega_p$ for ellipses with varying aspect ratios α for a true angular velocity of $\omega_p = -22.9°$. (e) Median relative error over the aspect ratio for varying regularization weighting parameters λ.

For all particles, a butterfly-shaped area of underestimation is visible, aligned with the main axes of the ellipse. The relative size of this underestimation area to the total ellipse area increases with decreasing aspect ratio α. This indicates that the underestimation of ω_p is affected by the aspect ratio, with higher aspect ratios improving the angular velocity estimate. Qualitatively, both the magnitude of the underestimation and the ratio of the total area to the underestimated areas decrease with increasing aspect ratio.

The shape of the areas of underestimation is likely related to the aperture problem (Heitz et al., 2010). This problem arises because borders of the particles closer to the particle centroid tend to move less perpendicularly to their intensity gradient as the aspect ratio decreases. In the extreme case of a circular particle ($\alpha = 1$), the rotational movement cannot be detected by optical flow methods due to the lack of distinguishable features. Consequently, particles with less smooth and more ragged features than ellipsoids are expected to be tracked more accurately by the wOFV method. Therefore, as the aspect ratio increases, the optical flow algorithm can better resolve the angular velocity, reducing the underestimation.

To quantify this observation for different regularization weighting parameters, the median relative error $\mathrm{med}(\Delta\omega_p/\omega_p)$ is plotted in Figure 5(e) for different aspect ratios and regularization weighting parameters. It can be observed that for all λ values the error decreases with increasing aspect ratio

and reaches its minimum at $\alpha = 6$ or 7. Furthermore, for $\alpha = 2$, all $\lambda \leq 10$ predict the angular velocity with approximately the same accuracy. The best performance is achieved at $\lambda = 10$, which is the best regularization weighting parameter across all aspect ratios. This suggests that while aspect ratio affects the accuracy of angular velocity estimation, the choice of λ can be made robustly, ensuring reliable performance of the wOFV method across a range of particle shapes. Such consistency is crucial for applications involving a variety of particle geometries, as it simplifies the parameter tuning process and increases the versatility of the method. The results computed with the highest regularization, $\lambda = 100$, differ from the other results. This behavior is caused by over-regularization, which results in oversmoothing of the gradients across the particle, which is especially necessary for computing large angular velocities for particles with small aspect ratios.

3.1.3. Combined translational and rotational motion

Finally, the combined motion of simultaneous translation and rotation is examined. In the previous sections, separate conclusions were drawn for translational and rotational motion. However, in order to reliably use wOFV in practical applications, it is necessary to increase the complexity of the synthetically generated data. Therefore, in this section we study the combined translational and rotational motion of ellipses. For other parameters, the reader is referred to Table 1.

Taking into account the previously discovered limitations of the algorithm, the displayed results only include samples where the ellipses in I_0 and I_1 overlap. We begin by investigating how the translational accuracy is influenced when it is overlaid with rotation. In Figure 6, the relative endpoint error ee_p, described by

$$ee_p = \frac{\sqrt{(\hat{\underline{u}}_p - \underline{u}_p)^2}}{\left|\underline{u}_p\right|}, \tag{8}$$

is depicted for translational and combined movements.

It can be observed that ee_p remains comparable for both cases up to a maximum regularization of $\lambda = 10$. Only at $\lambda = 100$ does the error of the combined motion significantly increase, while it continues to decrease for the translational test case. In addition, it is observed that at high regularization the endpoint error is strongly correlated with the magnitude of the angular velocity. In other words, the larger the superimposed rotational motion, the larger the error in the predicted velocity $\hat{\underline{u}}_p$. This behavior can be explained by considering the optimal regularization weighting parameter λ for pure translation, which is theoretically infinite due to the lack of required velocity gradients. However, when rotation is superimposed on translation, a gradient across the particle is expected, which must be captured by wOFV. Therefore, the choice of λ is limited, as observed earlier in Figure 4 for pure rotation. For combined motion, the translation error increases with the magnitude of the angular velocity because the velocity gradient across the particle becomes more

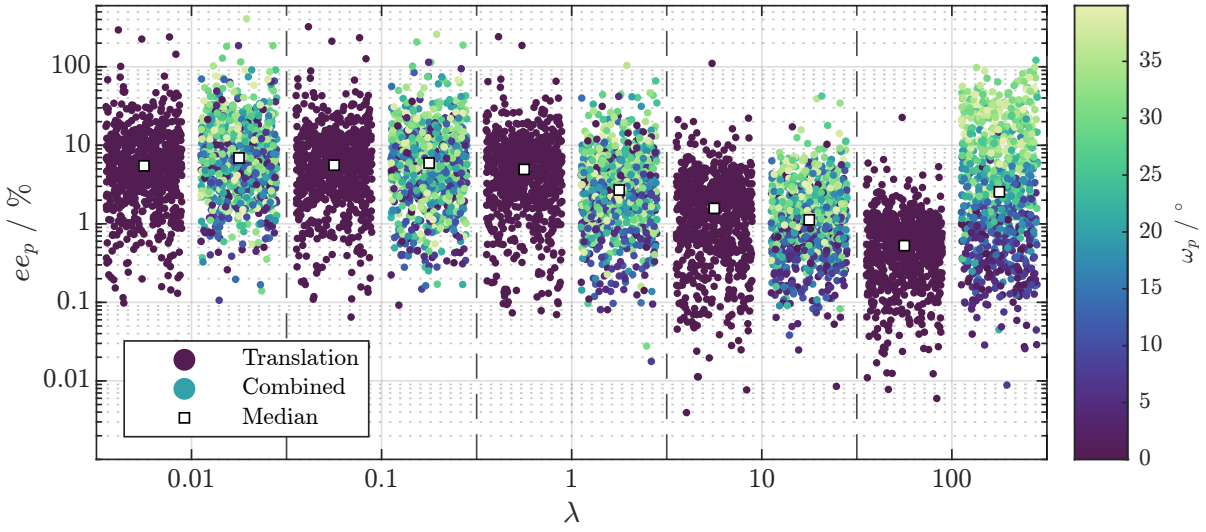

Figure 6. Evolution of the relative endpoint error distribution for increasing values of the regularization weighting parameter λ. Individual data points of $N = 1000$ samples are colored based on the angular velocity ω_p.

pronounced and must be accurately captured by the wOFV algorithm. Thus, while a higher λ may smooth out noise, it also runs the risk of oversmoothing critical gradients, leading to increased errors of translation motion estimation in cases of significant overlaid rotational motion.

After examining the translational accuracy, the rotational accuracy during combined motion is examined. These results are shown in Figure 7. Notably, the median relative error for all regularization levels is comparable to the pure rotational test case, and the error distribution is independent of the magnitude of the superimposed translational motion. For small levels of regularization, the median results are comparable across test cases, with a higher spread of results for smaller λ values, similar to pure rotational motion. However, for $\lambda \geq 10$ the error increases significantly. This indicates that while the wOFV algorithm performs well with low regularization for combined motion, higher regularization adversely affects the accuracy of rotational motion estimation due to the oversmoothing of necessary gradients.

In summary, the analysis of large particle motion using wOFV has revealed several important insights. For purely translational motion, higher regularization values λ significantly improve the accuracy of velocity estimation, provided that the particle images overlap between frames. This is due to the uniform nature of the flow field in translational motion, which benefits from the smoothing effect of higher regularization. In contrast, for purely rotational motion, the presence of velocity gradients around the center of rotation requires a careful balance in the choice of λ. Higher regularization leads to an underestimation of the angular velocity, while lower regularization can introduce non-physical outliers. The aspect ratio of the ellipsoids also plays a crucial role, with higher aspect ratios improving the accuracy of the angular velocity estimation by reducing the areas of underestimation caused by the aperture problem. Finally, in the case of combined transla-

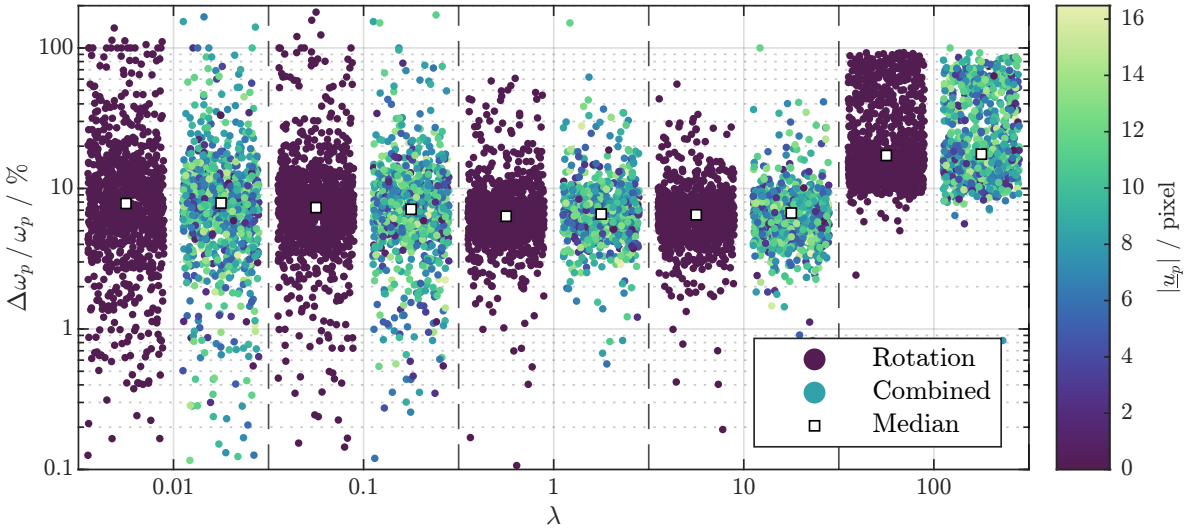

Figure 7. Evolution of the relative rotational error distribution for increasing values of the regularization weighting parameter λ. Individual data points of $N = 1000$ samples are colored based on the translational velocity $|\underline{u}_p|$.

tional and rotational motion, the results highlight the challenge of capturing both types of motion simultaneously. While wOFV performs well with low regularization, higher λ values lead to increased errors due to oversmoothing of critical velocity gradients. Overall, these results emphasize the importance of selecting an optimal regularization weighting parameter that balances the need for smoothness and the preservation of essential motion gradients, especially in complex motion scenarios involving both translation and rotation.

3.2. Multi-phase flow velocimetry analysis using DNS ground truth data

After analyzing large particle motions, we now investigate the ability of wOFV to extract turbulent flow fields in the vicinity of an aspherical particle from synthetic tracer images. Previous investigations have demonstrated the superior performance of wOFV over PIV using DNS ground truth data in homogeneous isotropic turbulence (Schmidt & Sutton, 2019) and wall-bounded turbulent flows (Nicolas et al., 2023). Recently, the authors applied wOFV to determine the turbulent flow surrounding walnut shell particles emerging from a turbulent round jet, where λ was chosen by verifying the correct physical reconstruction of the measured turbulent spectra due to the lack of a ground truth comparison (Geschwindner et al., 2024). However, the use of wOFV to determine the flow field around a dispersed particle, including a comparison to DNS-derived ground truth data, has not been reported. For this analysis, we use the DPFS data described in Section 2.3.

To render the DNS data, realistic experimental conditions were replicated (Geschwindner et al., 2023). The equivalent particle diameter was set to $D_{eq} = 150\,\mu\mathrm{m}$, with a pixel resolution of $5\,\mu\mathrm{m/px}$ in the final rendered image with dimensions of $390 \times 150\,\mathrm{px}$. The final particle density was set to

0.1 ppp (particles per pixel) based on the optimal value for wOFV reported in (Schmidt & Sutton, 2019). The ground truth was rendered assuming a laser light sheet thickness of 50 µm. The ellipse image was not included in the tracer images processed with wOFV and PIV as these are usually masked out using image discrimination algorithms (Khalitov & Longmire, 2002). Given the initial particle Reynolds number of approximately 1000, the movement of the ellipse was significantly slower than the fluid movement. This setup provides a preliminary assessment of the performance of wOFV and PIV in a multi-phase scenario without substantial simultaneous movement of the dispersed and carrier phases between frames. Future studies will explore this with lower Reynolds numbers.

In the following, an exemplary analysis of one vector field from DNS and its accuracy based on synthetic data is presented. Figure 8 compares the rendered ground truth, PIV with an optimal interrogation window size of $w = 12\,\mathrm{px}$ using an overlap of 75 % (processed in Lavision Davis 10.2), and wOFV with an optimal setting of $\lambda = 0.33$. These optimal settings are derived from error calculations, which will be discussed in detail in Fig. 9.

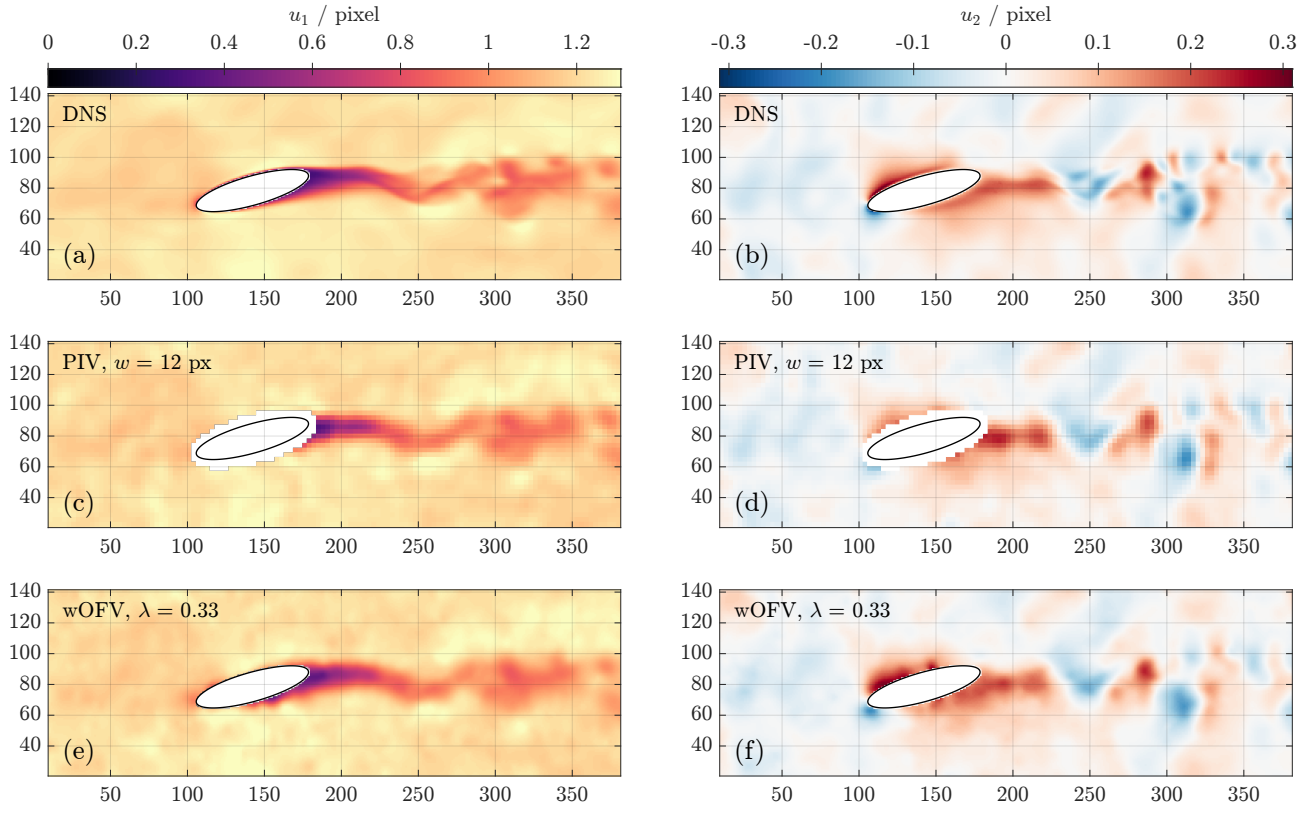

Figure 8. Comparison of flow fields in the u_1 (left column) and u_2 (right column) directions obtained from DNS (a, b), PIV with an interrogation window size of $w = 12\,\mathrm{px}$ (c, d), and wOFV with $\lambda = 0.33$ (e, f). Axis units are in pixels.

Both wOFV and PIV effectively capture the wake behind the particle under optimal conditions and show comparable flow fields, with wOFV showing slightly better resolution. This improved reso-

lution is particularly evident in the wake region, where vortices detach from the ellipsoid. While particle masking in PIV leads to unresolved structures near the particle surface, wOFV qualitatively reconstructs parts of the very thin boundary layer near the particle surface. This includes capturing the stagnation point at the leading tip of the ellipsoid and the flow along the elongated parts of the ellipsoid surface. The superior resolution of wOFV is easily seen in the dense motion field, as particularly well illustrated in Fig. 8(f) compared to Fig. 8(b), highlighting the clear advantage of wOFV over PIV. Future work will need to confirm these results when the ellipsoid motion is not negligibly small, especially for lower slip velocities and particle Reynolds numbers.

To quantitatively compare the performance of wOFV and PIV, the endpoint error distribution,

$$EE_i = \sqrt{(\hat{u}_{1,i} - u_1)^2 + (\hat{u}_{2,i} - u_2)^2}, \tag{9}$$

and the normalized root mean square error (RMSE),

$$\varepsilon_u = \sqrt{\frac{1}{n_v} \sum_i \frac{(\hat{u}_{1,i} - u_1)^2 + (\hat{u}_{2,i} - u_2)^2}{u_1^2 + u_2^2}}, \tag{10}$$

where n_v denotes the number of vectors per image, have been computed as shown in Fig. 9. For wOFV and PIV, the same masking of the particle and boundary regions was applied to ensure a fair comparison by excluding vectors close to the particle (ensuring that the same regions of the flow field are statistically compared). The highest values for EE are observed in the detachment zone directly behind the particle and in its wake where high flow gradients and vortices are present.

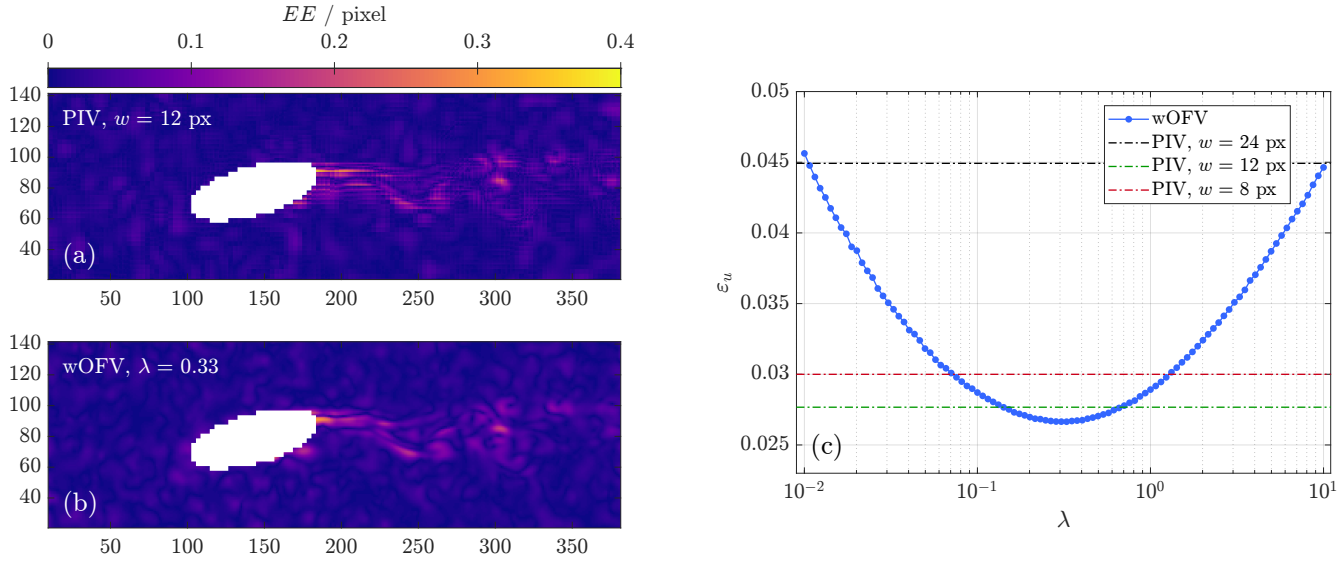

Figure 9. (a, b) Spatial distribution of the endpoint error EE for PIV and wOFV at an optimal value of $\lambda = 0.33$. (c) Normalized root mean square error ε_u for PIV and wOFV with respect to the regularization weighting parameter λ.

Fig. 9(c) shows ε_u for a wide range of λ values, with an optimum found at $\lambda = 0.33$. Notably, wOFV outperforms the PIV calculations using $w = 12\,\text{px}$ within the λ range of 0.14 to 0.66, with

an optimal value at 0.33. For PIV, different interrogation window sizes were investigated. It is apparent that decreasing the window size from 24 px to 12 px significantly lowers RMSE. However, further decreasing the window size of PIV to 8 px increases the error again, likely due to the lack of sufficient particles in the PIV correlation calculations. Even under optimal PIV settings, in the absence of image noise and with perfectly lit particles, wOFV outperforms PIV both quantitatively in providing more accurate results and qualitatively by resolving structures close to the particle surface. Future studies with lower slip velocities will examine this in more detail.

4. Conclusions

This study presented an evaluation of wavelet-based optical flow velocimetry (wOFV) for motion estimation of multi-phase flows. Here, the motion of dispersed ellipsoidal particles and their surrounding turbulent carrier flow were processed and studied based on synthetically generated image data.

In the first part of our work, the rigid motion of dispersed ellipses, consisting of translational and rotational components, was systematically evaluated from wOFV-generated dense motion fields. The results demonstrated the critical role of the regularization weighting parameter λ in accurately capturing the motion of elliptical particles. Higher values of λ improved translational motion estimation, while an optimal regularization weighting parameter setting for rotational motion was found that balanced under-regularization and the appearance of non-physical structures, as well as the over-blurring of gradients at high λ values, which must be avoided since the accurate capture of rotation inherently involves the resolution of a velocity gradient across the particle. The effect of aspect ratio on the accuracy of rotational motion estimation was highlighted, with higher aspect ratios resulting in less underestimation of angular velocity. In addition, wOFV maintained its accuracy in scenarios involving combined translational and rotational motion, especially when optimal regularization weighting parameters were used. The algorithm effectively resolved velocity gradients, which are critical for capturing combined motion.

The second part of the study aimed to capture the motion of the carrier phase turbulent flow surrounding an aspherical particle using wOFV, benchmarked with DNS data and compared to the state-of-the-art PIV. In this comparison, wOFV outperformed PIV in capturing finer structures near the particle surface and accurately representing the wake region. The superior resolution of wOFV was particularly evident in the dense motion fields, providing more accurate results even under ideal PIV conditions. Quantitative evaluations using endpoint error and normalized root mean square error analyses confirmed the advantage of wOFV over PIV. The performance of wOFV was optimal within a certain range of regularization weighting parameters.

In conclusion, wOFV proved to be a powerful tool for the analysis of multi-phase flow dynamics, offering higher resolution and accuracy compared to PIV, especially in complex flow scenarios in-

volving aspherical particles. Future studies focusing on lower slip velocities and varying Reynolds numbers will further elucidate the potential of wOFV in such applications. Furthermore, the simultaneous capture of multiple aspherical particles within an image frame represents an interesting extension of the scenario presented in this work.

Acknowledgements

This work is funded by DFG (Project number 215035359, SFB/TRR 129 Oxyflame: Development of methods and models to describe solid fuel reactions within an oxy-fuel atmosphere) and by ERC (grant 759546).

Nomenclature

a	Semi-major axis of the ellipse [px]
b	Semi-minor axis of the ellipse [px]
D_{eq}	Equivalent particle diameter
EE	Endpoint error [px]
$I(\underline{x}, t)$	Brightness intensity at position $\underline{x}$ and time t
J_D	Data term of the penalty function
J_R	Regularization term of the penalty function
k	Image size exponent for padding
n_v	Number of velocity vectors
$\underline{r}_{ci}$	Vector from position i to the center point [px]
$\underline{u}$	Velocity vector [px]
$\underline{\hat{u}}$	Estimated velocity vector [px]
$\underline{u}_p$	Particle velocity vector [px]
$\underline{\hat{u}}_p$	Estimated particle velocity vector [px]
u_1	Velocity component in the x-direction [px]
u_2	Velocity component in the y-direction [px]
ε_u	Normalized root mean square error (RMSE)
w	Interrogation window size [px]
x_c, y_c	Coordinates of the centroid [px]
α	Aspect ratio of the ellipse
λ	Regularization weighting parameter
ω_p	Angular velocity of the particle [°]
$\hat{\omega}_p$	Estimated angular velocity of the particle [°]
$\underline{\theta}$	Wavelet coefficients
Ψ	Discrete wavelet transform (DWT)

σ_{LS} Thickness of the laser sheet [µm]

References

Balachandar, S., & Eaton, J. K. (2010). Turbulent Dispersed Multiphase Flow. *Annual Review of Fluid Mechanics*, *42*(1), 111–133. doi: 10.1146/annurev.fluid.010908.165243

Batten, P., Goldberg, U., & Chakravarthy, S. (2004). Interfacing Statistical Turbulence Closures with Large-Eddy Simulation. *AIAA Journal*, *42*(3), 485–492. doi: 10.2514/1.3496

Dérian, P., Héas, P., Herzet, C., & Mémin, E. (2013). Wavelets and Optical Flow Motion Estimation. *Numerical Mathematics: Theory, Methods and Applications*, *6*(1), 116–137. doi: 10.4208/nmtma.2013.mssvm07

Fröhlich, K., Meinke, M., & Schröder, W. (2020). Correlations for inclined prolates based on highly resolved simulations. *Journal of Fluid Mechanics*, *901*. doi: 10.1017/jfm.2020.482

Geschwindner, C., Nicolas, A., Westrup, K., Dreizler, A., Peterson, B., & Böhm, B. (2024). Resolving biomass-turbulence interactions at the particle scale using ultra-high-speed wavelet-based optical flow velocimetry (wOFV). *Proceedings of the Combustion Institute*, accepted for oral presentation.

Geschwindner, C., Westrup, K., Dreizler, A., & Böhm, B. (2023). Pulse picking of a fiber laser enables velocimetry of biomass-laden jets at low and ultra-high repetition rates. *Proceedings of the Combustion Institute*, *39*(1), 1325–1335. doi: 10.1016/j.proci.2022.07.138

Hartmann, D., Meinke, M., & Schröder, W. (2011). A strictly conservative Cartesian cut-cell method for compressible viscous flows on adaptive grids. *Computer Methods in Applied Mechanics and Engineering*, *200*(9-12), 1038–1052. doi: 10.1016/j.cma.2010.05.015

Heitz, D., Mémin, E., & Schnörr, C. (2010). Variational fluid flow measurements from image sequences: synopsis and perspectives. *Experiments in Fluids*, *48*(3), 369–393. doi: 10.1007/s00348-009-0778-3

Horn, B. K., & Schunck, B. G. (1981). Determining optical flow. *Artificial Intelligence*, *17*(1-3), 185–203. doi: 10.1016/0004-3702(81)90024-2

Jassal, G. R., & Schmidt, B. E. (2023). Accurate near-wall measurements in wall bounded flows with optical flow velocimetry via an explicit no-slip boundary condition. *Measurement Science and Technology*, *34*(12), 125303. doi: 10.1088/1361-6501/acf872

Kadri-Harouna, S., Dérian, P., Héas, P., & Mémin, E. (2013). Divergence-Free Wavelets and High Order Regularization. *International Journal of Computer Vision*, *103*(1), 80–99. doi: 10.1007/s11263-012-0595-7

Kähler, C. J., Scharnowski, S., & Cierpka, C. (2012). On the resolution limit of digital particle image velocimetry. *Experiments in Fluids*, *52*(6), 1629–1639. doi: 10.1007/s00348-012-1280-x

Khalitov, D. A., & Longmire, E. K. (2002). Simultaneous two-phase PIV by two-parameter phase discrimination. *Experiments in Fluids*, *32*(2), 252–268. doi: 10.1007/s003480100356

Nicolas, A., Zentgraf, F., Linne, M., Dreizler, A., & Peterson, B. (2023). Assessment and application of wavelet-based optical flow velocimetry (wOFV) to wall-bounded turbulent flows. *Experiments in Fluids*, *64*(3), 50. doi: 10.1007/s00348-023-03594-y

Panahi, A., Vorobiev, N., Schiemann, M., Tarakcioglu, M., Delichatsios, M., & Levendis, Y. A. (2019). Combustion details of raw and torrefied biomass fuel particles with individually-observed size, shape and mass. *Combustion and Flame*, *207*, 327–341. doi: 10.1016/j.combustflame.2019.06.009

Raffel, M., Willert, C. E., Scarano, F., Kähler, C. J., Wereley, S. T., & Kompenhans, J. (2018). *Particle Image Velocimetry*. Cham: Springer International Publishing. doi: 10.1007/978-3-319-68852-7

Schmidt, B. E., & Sutton, J. A. (2019). High-resolution velocimetry from tracer particle fields using a wavelet-based optical flow method. *Experiments in Fluids*, *60*(3). doi: 10.1007/s00348-019-2685-6

Schmidt, B. E., & Sutton, J. A. (2020). Evaluation of gas- and particle-phase separation methods for velocity measurements in turbulent multiphase flows. *Experiments in Fluids*, *61*(12). doi: 10.1007/s00348-020-03082-7

Schneiders, L., Günther, C., Meinke, M., & Schröder, W. (2016). An efficient conservative cut-cell method for rigid bodies interacting with viscous compressible flows. *Journal of Computational Physics*, *311*, 62–86. doi: 10.1016/j.jcp.2016.01.026

Schneiders, L., Meinke, M., & Schröder, W. (2017). Direct particle–fluid simulation of Kolmogorov-length-scale size particles in decaying isotropic turbulence. *Journal of Fluid Mechanics*, *819*, 188–227. doi: 10.1017/jfm.2017.171

Voth, G. A., & Soldati, A. (2017). Anisotropic Particles in Turbulence. *Annual Review of Fluid Mechanics*, *49*(1), 249–276. doi: 10.1146/annurev-fluid-010816-060135